High performance Al/TiB2 composites fabricated by nanoparticle reinforcement and cutting-edge super vacuum assisted die casting process

Xixi Dong, Hamza Youssef, Yijie Zhang, Shihao Wang, Shouxun Ji*

Brunel Centre for Advanced Solidification Technology (BCAST), Brunel University London, Uxbridge UB8 3PH, United Kingdom

*Corresponding author: Tel: +44 1895 266663; Fax: +44 1895 269758

E–mail address: shouxun.ji@brunel.ac.uk

Abstract

The enhancement of double strengthening by nanoparticles and nanoscale precipitates in die-cast Al–Si–Mg–Mn–TiB_2 composites has be achieved by introducing TiB_2 nanoparticles into Al-*Si-*Mg alloy fabricated by super vacuum assisted high pressure die casting process. The composite with 3.5wt.% TiB_2 nanoparticles could deliver the hardness of 1.5 GPa, the yield strength of 351 MPa and ultimate tensile strength of 410 MPa in association with an industrially applicable ductility of 5.2 %, after solution and peak ageing heat treatment. The TiB_2 nanoparticles distributed at the grain boundaries rather than in the α–Al matrix of the composites in as-cast state. After solution and peak ageing, the TiB_2 nanoparticles were enrolled into the α–Al matrix through the combining and coarsening of the α–Al phase during heat treatment, and nanoscale β″ precipitates formed in the α–Al matrix. Both the TiB_2 nanoparticles and the nanoscale β″ precipitates had highly coherent interfaces with the α–Al matrix, i.e., Al(11-1)//TiB_2(0001), Al[011]//TiB_2[11-20], Al[320]//β"(*a*-axis), Al[1-30]//β"(*c*-axis) and Al(020)//β"(*b*-axis), confirming strong interfacial strengthening. The double strengthening of the TiB_2 nanoparticles and the nanoscale β″ precipitates dispersing in the α–Al matrix resulted in the milestone high strength of the composites.

Key words: Aluminium composites; Microstructures, Mechanical properties; High pressure die casting; Nano particles.

1. Introduction

The application of thin-wall component in transport manufacturing has been recognised as an effective method to reduce the structure weight and the green gas emissions resulted from the reducing burn of fuels. To achieve the manufacturing of thin-wall components, high pressure die casting (HPDC) has been widely used in producing aluminium and magnesium alloy components because of the advantages of high dimensional accuracy, high production efficiency, and considerable economic benefits [3–6]. In recent years, the world-wide interesting requires the die-cast aluminium alloys to provide high strength and high ductility in order to achieve thin wall components.

The currently available die-cast aluminium alloys can be basically divided into two groups, one can provide good yield strengths, and the other can provide excellent ductility. The alloys based on Al-Si-Cu and Al-Si-Mg usually offer a yield strength of ~130–170 MPa in association with a ductility of ~4–5 % under as-cast condition [9,10]. After heat treatment, the yield can be increased to **. The alloys based on the Al-Si-Mg and Al-Mg-Si can provide an elongation greater than 15%, which can still be adjusted through heat treatment. From these, it is clear that the development of aluminium alloys needs to be able to either increase the yield strength or increase the elongation.

In order to increase the yield strength, the micro alloying method has been applied, but the achievable yield strengths are still in the relatively low level of 180–190 MPa [11–14]. Meanwhile, the particle reinforcement method was proved to be effective for strengthening cast aluminium alloys [15,16]. For cast aluminium alloys, ceramic particles such as TiB_2, Al_2O_3, Si_3N_4, B_4C, TiC and SiC have been added as strengthening phases [17–22]. However, few literatures reported the particle reinforcement of the die-cast aluminium alloys under HPDC [23], partially because of the capability and castability of these materials. Among the available ceramic reinforcement particles for casting, TiB_2 wets with molten aluminium, and can be in-situ synthesised in the molten aluminium with a size of nanoscale and applicable for HPDC [24]. So TiB_2 nanoparticles can be chosen to reinforce the die-cast aluminium alloys. Moreover, the super vacuum assisted HPDC process developed recently can achieve a high vacuum of ~20 mbar [25], which is far below the vacuum level of ~50–100 mbar obtained by the conventional vacuum assisted HPDC process [26–29], and it can largely decrease the gas porosities in HPDC castings and enable the further strengthening of the die-cast aluminium alloys through heat treatment.

From the developed HPDC aluminium alloys, Al–Si–Mg alloys have been widely used for the manufacturing of high integrity castings with a combination of good castability, strength, ductility and corrosion resistance [30–32]. However, 310 MPa was nearly the upper limit of the yield strength of the Al–Si–Mg cast alloy system [33]. This is mainly because that the application of strengthening mechanisms in Al-Si-Ma alloys rely on sulition strengthening, precipitate strengthening, grain size strengthening and weak secondary phase strengthening. In order to increase the yield strength of die-cast aluminium alloys, it is essential to enhance the strengthening by an effect and innovate way that was not used before.

Therefore, in the present study, we aim employ a double strengthening mechanism to enhance the die cast materials to offer higher yield strength with a good elongation. TiB_2 nanoparticles were added into the Al–Si–Mg–Mn alloy melt to introduce extra strengthening phase without significantly sacrificing the castability on top of the existing strengthening mechnisims in the alloy. BY doing this the die-cast Al–Si–Mg–Mn–TiB_2 composites can provide a yield strength above 350 MPa with the industrially applicable ductility of over 4 %. The processing characterisations is introduced for ***. The discussion focus on the double strengthening in the materials.

2. Experimental

2.1. Materials preparation

The die-cast Al–Si–Mg–Mn–TiB_2 composites reinforced by TiB_2 nanoparticles, with the actual compositions (in wt.%) of Al–9Si–0.6Mg–0.6Mn–0.18Fe–0.12Ti–xTiB_2 (x=0, 1.5, 3.5), were melted in a clay-graphite crucible using the electric resistance furnace. The commercial purity pure ingot of Al was first melted in the crucible, then the pure ingot of Mg and the master alloys of Al–50 wt.% Si, Al–20 wt.% Mn, Al–45 wt.% Fe and Al–10 wt.% Ti were added into the molten Al to achieve the designed composition. After the TiB_2 ceramic nanoparticles with the desired amounts were added into the melt through the addition of the Al–10 wt.% TiB_2 master alloy. The details of the TiB_2 nanoparticles in the Al–10 wt.% TiB_2 master alloy are presented in Section 3.1. During melting, the temperature of the furnace was controlled at 750 °C. After melting, the Al–10 wt.% Sr master alloy was added into the melts to achieve the desired Sr content of 200 ppm, for the modification of the morphology of the eutectic Si phase during solidification. Then the melts were degassed through injecting pure argon into the melts by using a rotary degassing impeller at a speed of 350 rpm for 5 min. After degassing, the melts were stirred mechanically for the homogenisation of the TiB_2

nanoparticles in the alloy melts, and the melts were ready for the super vacuum assisted HPDC subsequently.

2.2. Two-stage super vacuum assisted HPDC

Fig. 1a shows the two-stage super vacuum assisted HPDC process applied for the fabrication of the present die-cast Al–Si–Mg–Mn–TiB_2 composites. Different from the generally used one-stage vacuum by evacuation only from the die cavity, here the two-stage vacuum was applied by evacuation from both the shot sleeve and the die cavity simultaneously, and the super vacuum of ~20 mbar was obtained in limited evacuation time, which was far below the commonly achieved vacuum of ~50–100 mbar by the one-stage evacuation process [26–29]. The details of the two-stage evacuation process were introduced in our latest report [25]. Eight ASTM B557 standard round tensile test bars with a gauge dimension of ϕ6.35 mm × 50 mm were casted in the die cavity under each HPDC shot, as shown in Fig. 1a. The HPDC experiments were conducted on a 4500 kN cold chamber HPDC machine. Fig. 1b presents one stage of the vacuum channel set at the shot sleeve, and Fig. 1c shows the other stage of the vacuum channel set at the top of the die cavity. The HPDC die was heated by the circulation of mineral oil, and the die temperature was controlled at ~95 °C. The prepared alloy melts were loaded into the shot sleeve for HPDC, and the pouring temperature of the melts was controlled at 690 °C. The holding pressure during HPDC was controlled at 320 bar.

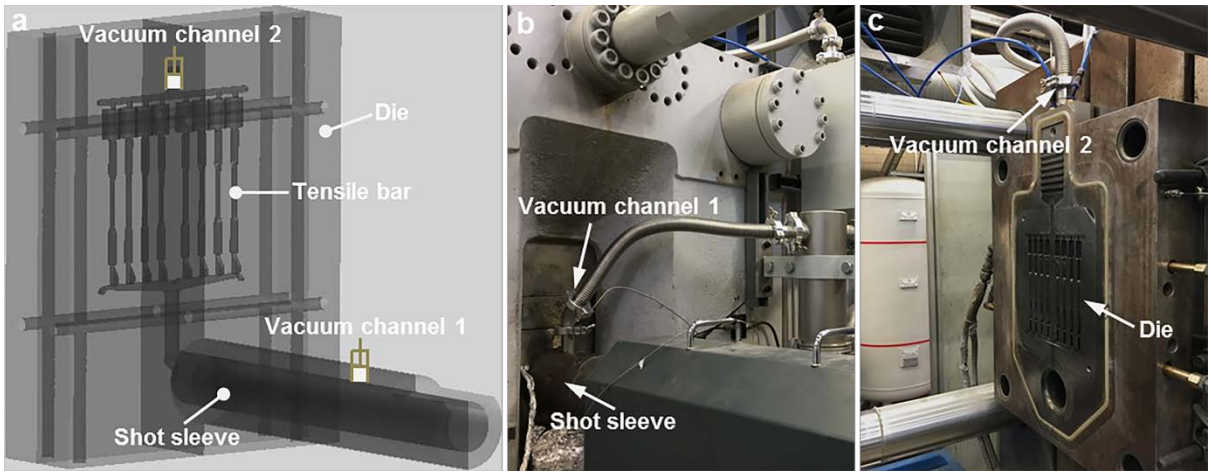

Fig. 1. The set-up of die and vacuum for the two-stage super vacuum assisted high pressure die casting of the die-cast Al–Si–Mg–Mn–TiB_2 composites. (a) Schematic showing the ASTM B557 standard round tensile test bars casted under super vacuum assisted high pressure die casting, (b) Vacuum channel 1 evacuated from the shot sleeve, (c) Vacuum channel 2 evacuated from the die cavity.

2.3. Heat treatment and tensile tests

The as-cast tensile test bars fabricated by super vacuum assisted HPDC were subjected to T6 heat treatment, which included the solid solution treatment and the subsequent peak artificial ageing. Solution treatment was conducted at 540 °C for 30 min, followed by immediate water quenching. Ageing treatment was carried out at 170 °C for different time, followed by air cooling. Vickers hardness tests were conducted on a FM-800 tester with an applied load of 10 kg for 10 s, to determine the peak ageing time. The T6 heat-treated tensile test bars were pulled on an Instron 5500 machine at room temperature. The extensometer with a gauge length of 50 mm was applied for the monitoring of the strain during tensile tests. The ramp rate for extension was set as 1 mm/min. Each tensile data reported with standard deviation was based on the testing of at least twelve samples.

2.4. Microstructure characterization

The microstructure was examined using the Zeiss SUPRA 35VP scanning electron microscope (SEM) equipped with electron backscatter diffraction (EBSD), and the JEOL-2100 transmission electron microscopy (TEM). The microstructure characterization of the samples was taken from the gauge length section of the tensile test bars. The samples for SEM morphology analysis were prepared following the standard grinding and polishing process, and then etching with the standard Keller's solution. The samples for EBSD analysis were prepared by vibration polishing at a frequency of 90 Hz for three hours after the standard grinding and polishing. The tensile fracture analysis was also performed via SEM. Thin specimens for TEM observation were prepared by ion beam polishing on a Gatan Precision Ion Polishing System (PIPS, Gatan model 691). A constant preparation temperature of -10 °C was maintained during the ion beam polishing. TEM operating at 200 kV was used for bright-field imaging, select area diffraction pattern (SADP) analysis and high-resolution transmission electron microscopy (HRTEM) imaging.

3. Results & discussion

3.1. Al–TiB_2 master alloy

The Al–10wt.%TiB_2 master alloy was synthesised through the in-situ reaction between the K_2TiF_6 and KBF_4 salts in the molten Al at a high temperature of ~850 °C [36]. The TiB_2 ceramic nanoparticles were formed during the reaction, and remained in the Al–10wt.%TiB_2 master alloy after solidification. Fig. 2a presents the SEM morphology of the Al–10wt.%TiB_2 master alloy, and TiB_2 nanoparticles were found dispersing homogeneously in the Al matrix of the master alloy. The TiB_2 nanoparticles were reported in the shape of the hexagonal

prisms with hexagonal close packed lattice structure, and the TiB_2 nanoparticles were facetted with basal {0001} and prismatic {1100} facets [37]. From Fig. 2a, most of the TiB_2 nanoparticles were observed lying on the Al matrix with exposing {1100} prismatic facets, as the TiB_2 nanoparticles with the basal {0001} facets embedded in the Al matrix were washed away by water during the clean process after etching. Fig. 2b shows the bright-field TEM morphology of the TiB_2 nanoparticle in the Al–10wt.%TiB_2 master alloy. Fig. 2c presents the SADP of the TiB_2 nanoparticle in Fig. 2b, and Fig. 2d shows the HRTEM image of the TiB_2 nanoparticle in Fig. 2b, which verified that the nanoparticles dispersed in the Al–10wt.%TiB_2 master alloy were TiB_2. The TiB_2 nanoparticles are ceramic phases with a high melting point of 3230 °C, and the TiB_2 nanoparticles are stable phases that don′t react with molten Al after the formation through in-situ reaction. It is easier to add the TiB_2 nanoparticles into the Al melts through the Al–TiB_2 master alloy rather than the pure TiB_2 powders. Thus the TiB_2 nanoparticles were the stable reinforcement phases that were added into the designed die-cast Al–Si–Mg–Mn alloy melts through the Al–10wt.%TiB_2 master alloy, for the achieving of high performance die-cast Al–Si–Mg–Mn–TiB_2 composites.

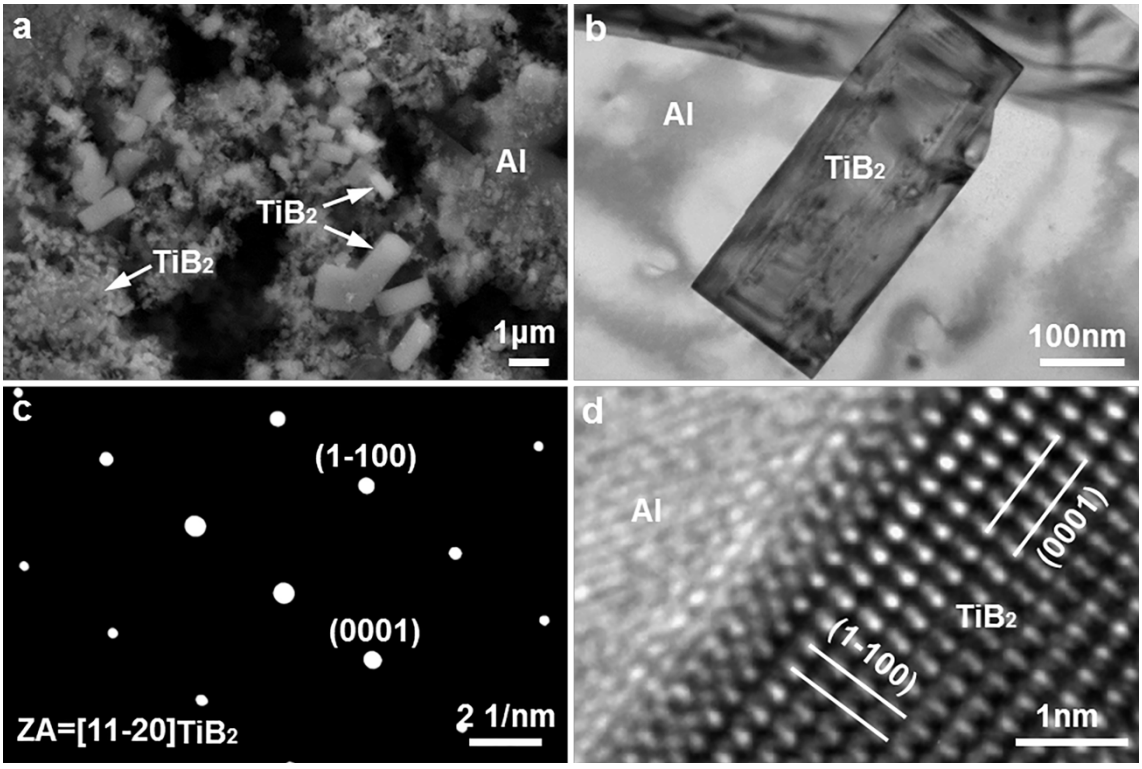

Fig. 2. SEM and TEM micrographs showing the TiB_2 nanoparticles in the Al–10wt.%TiB_2 master alloy. (a) Morphology and distribution of TiB_2 nanoparticles under SEM observation, (b) Bright-field TEM morphology of TiB_2 nanoparticle, (c) SADP and (d) HRTEM image of the TiB_2 nanoparticle in (b).

3.2. As-cast Al–Si–Mg–Mn–TiB_2 composites

3.2.1. Casting and die-cast capability

Fig. 3 presents the castings of the ASTM B557 standard round tensile test bars fabricated under super vacuum assisted HPDC. Fig. 3a shows the casting of the Al–Si–Mg–Mn die-cast alloy without TiB_2 reinforcement, and the casting was well filled with high integrity and no hot-tearing crack, indicating the good die-cast capability of the Al–Si–Mg–Mn base alloy. Fig. 3b presents the casting of the 1.5wt.% TiB_2 reinforced composite, and the integrity of the casting was similar to that of the base alloy, indicative of the good die-cast capability of the Al–Si–Mg–Mn–1.5wt.% TiB_2 composite. Fig. 3c shows the casting of the 3.5wt.% TiB_2 reinforced composite, and the casting was still well filled to the very thin chill vent end with good integrity and no hot-tearing crack, indicating the good die-cast capability of the Al–Si–Mg–Mn–3.5wt.% TiB_2 composite. The addition of the nano reinforcement particles could decrease the fluidity of the alloy melt, and the slight decrease of the chill vent height in the castings of the TiB_2 reinforced composites comparing with the base alloy was due to the minor decrease of the fluidity of the alloy melts. The high content of silicon ensured the good fluidity and low solidification temperature range and thermal expansion of the base alloy, which were beneficial to the die filling and hot-tearing resistance of the base alloy, and this led to the good die-cast capability of the base alloy. The good die-cast capability of the base alloy and the limited addition of TiB_2 nanoparticles within 3.5wt.% resulted in the good die-cast capability of the present Al–Si–Mg–Mn–TiB_2 composites.

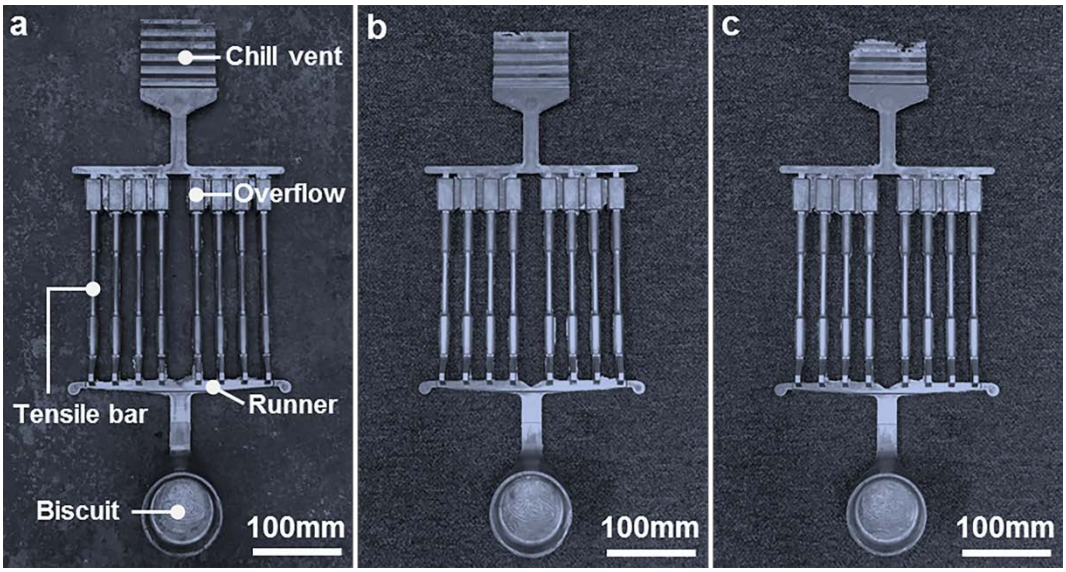

Fig. 3. Castings of the ASTM B557 standard round tensile test bars fabricated under super vacuum assisted high pressure die casting. (a) 0wt.% TiB_2 reinforced alloy, (c) 1.5wt.% TiB_2 reinforced composite, (d) 3.5wt.% TiB_2 reinforced composite.

3.2.2. As-cast microstructure

Figs. 4a and b show the SEM morphology of the as-cast Al–Si–Mg–Mn die-cast alloy without TiB_2 reinforcement. The microstructure of the alloy comprised the α–Al phase, the eutectic Si phase and the intermetallic phases of α–Fe and β–Mg_2Si. The α–Al phase was in two different sizes, i.e., the relatively coarse primary α_1–Al phase solidified in the shot sleeve with lower cooling rate and the fine secondary α_2–Al phase solidified in the die cavity with higher cooling rate. The eutectic Si phase was in fibrous morphology due to the modification effect of the element Sr [33,38]. The β–Mg_2Si intermetallic phase distributed in the grain boundary of the α–Al phase, and it was in block shape. Fig. 4c presents the SEM morphology of the as-cast Al–Si–Mg–Mn–1.5wt.% TiB_2 composite, TiB_2 nanoparticles were observed in the eutectic area that was in the grain boundary. The eutectic Si phase was also in fibrous morphology, and the α–Fe intermetallic phase was in faceted morphology. Fig. 4d shows the SEM morphology of the as-cast Al–Si–Mg–Mn–3.5wt.% TiB_2 composite, TiB_2 nanoparticles were also observed in the eutectic area that was in the grain boundary, and the amount of the TiB_2 nanoparticles in the grain boundary of the 3.5wt.% TiB_2 reinforced composite was higher than that of the 1.5wt.% TiB_2 reinforced composite. The size of the faceted α–Fe intermetallic phase was ~0.5–1 μm.

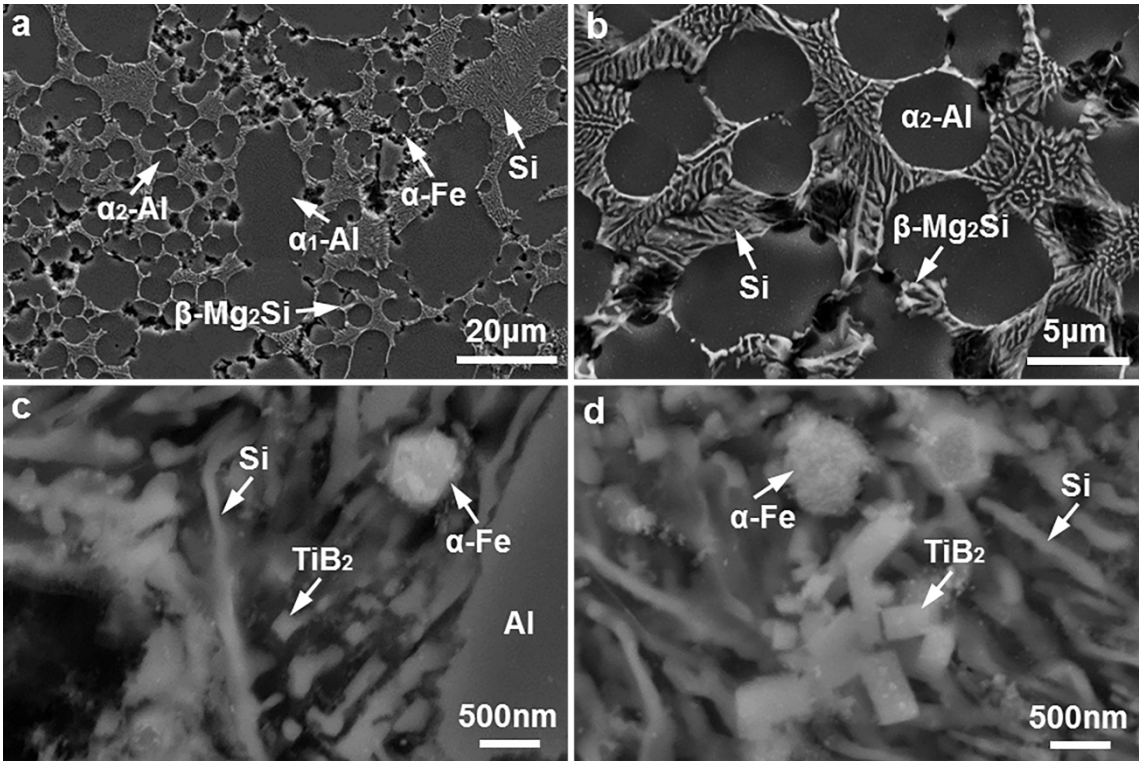

Fig. 4. SEM micrographs showing the microstructure of the die-cast Al–Si–Mg–Mn–TiB_2 composites in as-cast state. (a,b) 0wt.% TiB_2 reinforced alloy, (c) 1.5wt.% TiB_2 reinforced composite, (d) 3.5wt.% TiB_2 reinforced composite.

The intermetallic phase of β was rich in Mg and Si, and the intermetallic phase of α–Fe was rich in Al, Fe, Mn and Si, according to the energy dispersive X-ray spectroscopy (EDS) analysis under SEM. However, it was hard to determine the chemical formula and structure of the intermetallic phases under SEM, as the measurement accuracy of the element content was not high enough. TEM analysis was applied to confirm the β and α–Fe intermetallic phases in the present composites. Fig. 5a presents the bright-field TEM morphology of the β phase, and the SADP analysis result in Fig. 5b verified that the β phase was the Mg_2Si phase with the face centred cubic lattice structure. The lattice parameter of the β phase was determined as 0.638 nm from the (200) interplanar spacing of 0.319 nm measured in Fig. 5b, which agreed well with the reported lattice parameter of 0.639 nm of the β–Mg_2Si phase [39]. Fig. 5c shows the bright-field TEM morphology of the α–Fe phase, and the SADP analysis result in Fig. 5d confirmed that the α–Fe phase was the $Al_{15}(Fe,Mn)_3Si_2$ phase with the body centred cubic lattice structure. The lattice parameter of the α–Fe phase was determined as 1.270 nm from the (0-11) interplanar spacing of 0.898 nm measured in Fig. 5d, which agreed well with the reported lattice parameter of 1.270 nm of the $Al_{15}(Fe,Mn)_3Si_2$ phase [40].

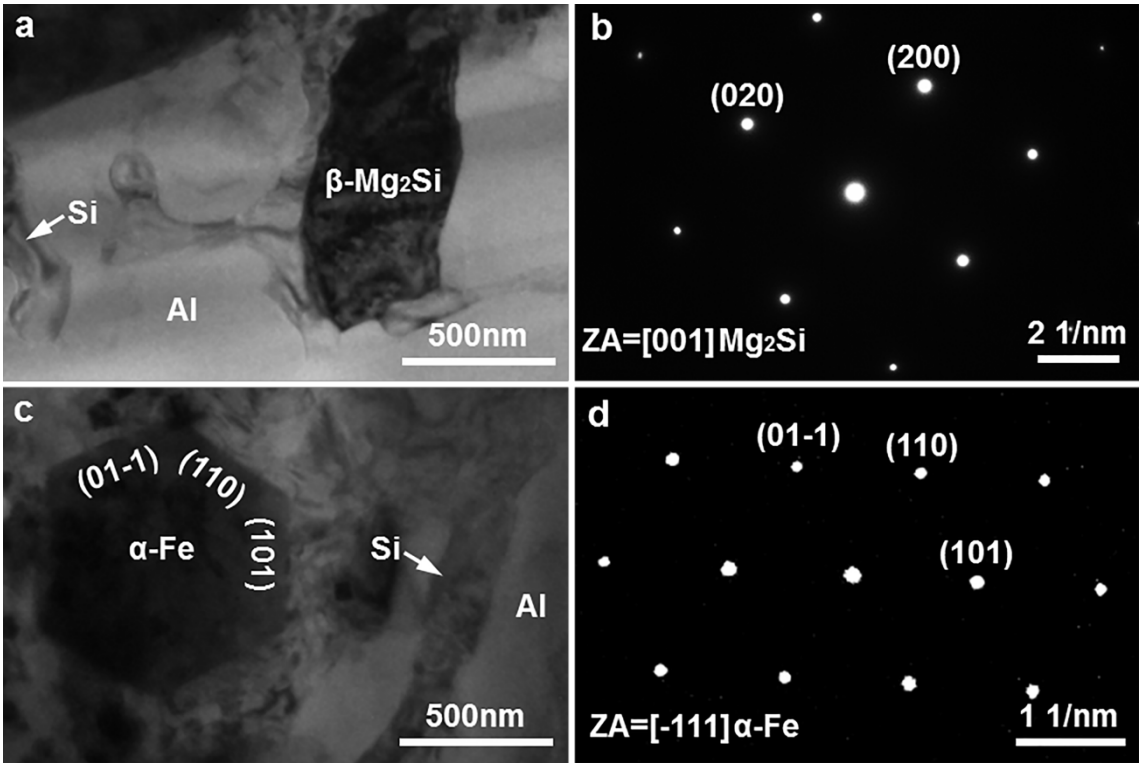

Fig. 5. TEM micrographs confirming the intermetallic phases in the die-cast Al–Si–Mg–Mn–TiB_2 composites in as-cast state. (a) Bright-field TEM image of the β–Mg_2Si intermetallic phase, (b) SADP of the β–Mg_2Si phase in (a), (c) Bright-field TEM image of the α–Fe intermetallic phase, (d) SADP of the α–Fe phase in (c).

Fig. 6 presents the bright-field TEM micrographs showing the distribution of the TiB_2 nanoparticles in the as-cast die-cast Al–Si–Mg–Mn–TiB_2 composites. Figs. 6a and b show the TEM morphology of the 1.5wt.% TiB_2 reinforced composite in as-cast state, and the TiB_2 nanoparticles distributed in the grain boundary (GB) of the α–Al phase. The matrix of the α–Al phase was clean, and hardly did the TiB_2 nanoparticles present in the α–Al grain. Figs. 6c and d present the TEM morphology of the 3.5wt.% TiB_2 reinforced composite in as-cast state, and the TiB_2 nanoparticles also distributed in the grain boundary rather than in the α–Al grain. The amount of the TiB_2 nanoparticles in the grain boundary of the 3.5wt.% TiB_2 reinforced composite was higher than of the 1.5wt.% TiB_2 reinforced composite. The distribution of the TiB_2 reinforcement nanoparticles in the grain boundary rather than in the α–Al matrix was also reported in the laser additive manufacturing of aluminium alloy [41], which had similar high cooling rate during solidification with the present HPDC process.

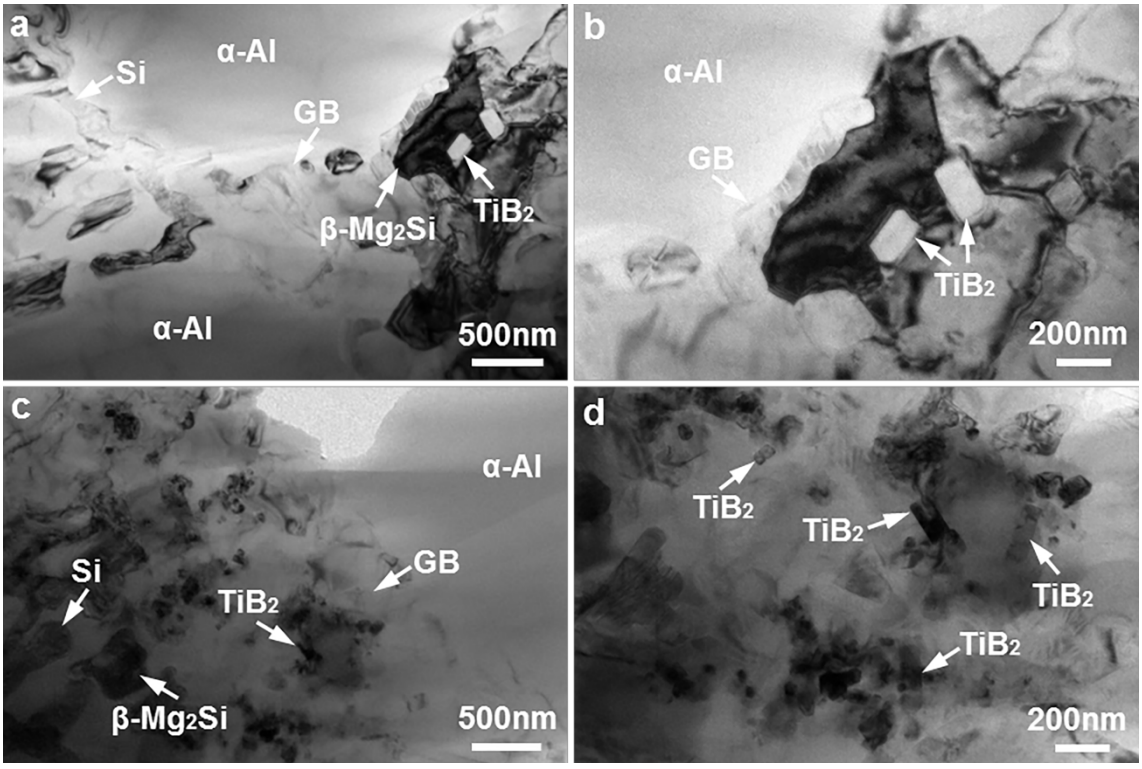

Fig. 6. Bright-field TEM micrographs showing the distribution of the TiB_2 nanoparticles in the as-cast die-cast Al–Si–Mg–Mn–TiB_2 composites. (a) 1.5wt.% TiB_2 reinforced composite, (b) Enlarged morphology of the TiB_2 nanoparticles in the grain boundary (GB) in (a), (c) 3.5wt.% TiB_2 reinforced composite, (d) Enlarged morphology of the TiB_2 nanoparticles in the grain boundary in (c).

3.3. Heat treatment of Al–Si–Mg–Mn–TiB_2 composites

Figs. 7a and b show the SEM morphology of the die-cast Al–Si–Mg–Mn alloy after solution heat treatment. The fibrous eutectic Si phase in the as-cast alloy was spheroidized

into the fine spheroidal Si particles after solution treatment, and the spheroidized Si particles distributed in the grain boundary of the α–Al matrix phase. The β intermetallic phase was hardly observed in the solution treated alloy, which indicated that the β phase in the grain boundary of the as-cast alloy was well dissolved into the α–Al matrix after the solution treatment. Fig. 7c presents the bright-field TEM morphology of the die-cast Al–Si–Mg–Mn alloy after solution heat treatment, and the SADP in Fig. 7d verified that the spheroidized particle in Fig. 7c was the Si phase. The lattice parameter of the Si phase was determined as 0.544 nm from the (111) interplanar spacing of 0.314 nm measured in Fig. 7d, which agreed well with the lattice parameter of 0.543 nm of the Si phase with diamond cubic structure. The spheroidization of the eutectic Si phase during solution treatment was also reported by previous studies on Al–Si based cast alloys [33,35,38], and the dissolving of the β phase into the α–Al matrix was due to the high temperature diffusion during solution treatment.

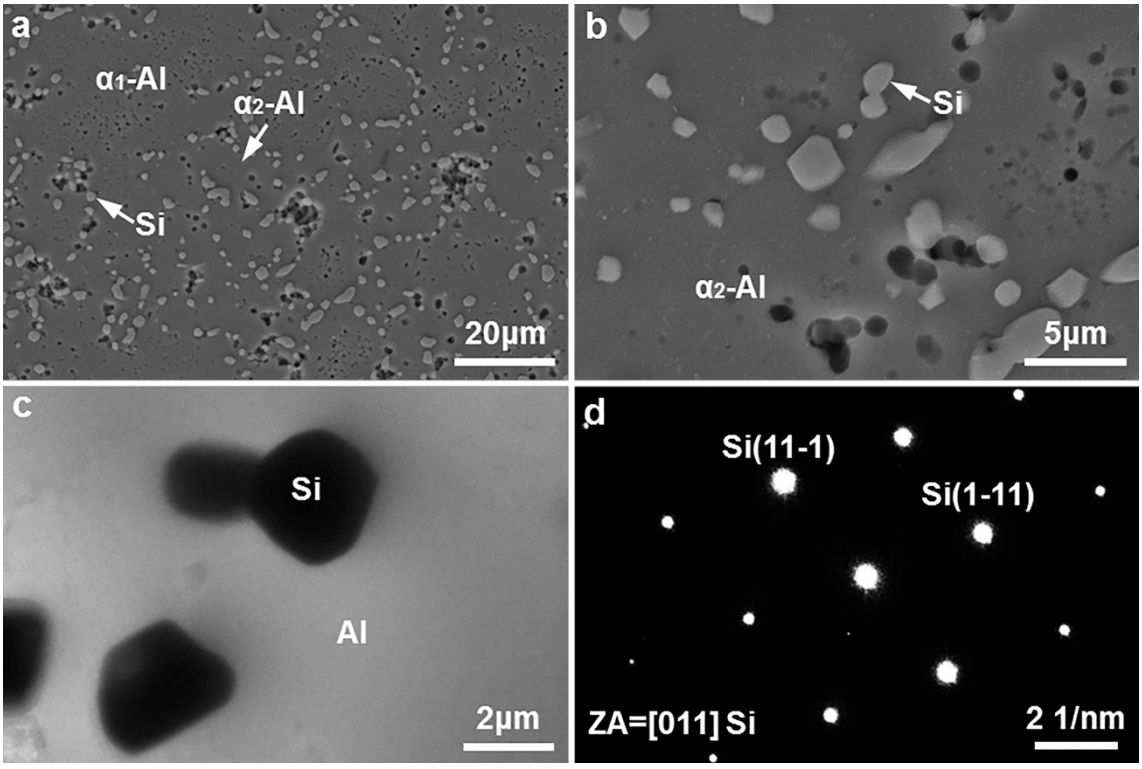

Fig. 7. SEM and TEM micrographs showing the microstructure of the die-cast Al–Si–Mg–Mn alloy after solution heat treatment. (a) Low magnification SEM morphology, (b) Enlarged SEM morphology, (c) Bright-field TEM morphology of the spheroidized Si phase, (d) SADP of the Si phase in (c).

Fig. 8 presents the evolution of the hardness of the die-cast Al–Si–Mg–Mn–TiB_2 composites versus ageing time after solution treatment. With the increase of the ageing time, the hardness first increased till reached the peak due to the precipitation of the fine nanoscale precipitates, and decreased subsequently resulting from the transformation of the fine

nanoscale precipitates into the relatively coarser nanoscale precipitates. The fine nanoscale precipitates are coherent with the Al matrix and have the strongest precipitation strengthening effect, while the coarsened nanoscale precipitates are not well coherent with the Al matrix and have relatively weaker precipitation strengthening effect. The hardness of the 0wt.% TiB_2 reinforced alloy reached the peak at the ageing time of 6 h, while the hardness of the 1.5wt.% TiB_2 and 3.5wt.% TiB_2 reinforced composites reached the peak at the ageing time of 8 h. The hardness of the solution and ageing heat-treated composites increased with increasing content of TiB_2, and the peak hardness of the 3.5wt.% TiB_2 reinforced composite was as high as 1.502 GPa. The peak ageing hours of 6 h, 8 h and 8 h were chosen as the final optimized ageing time for the 0wt.% TiB_2, 1.5 wt.% TiB_2 and 3.5wt.% TiB_2 reinforced composites respectively.

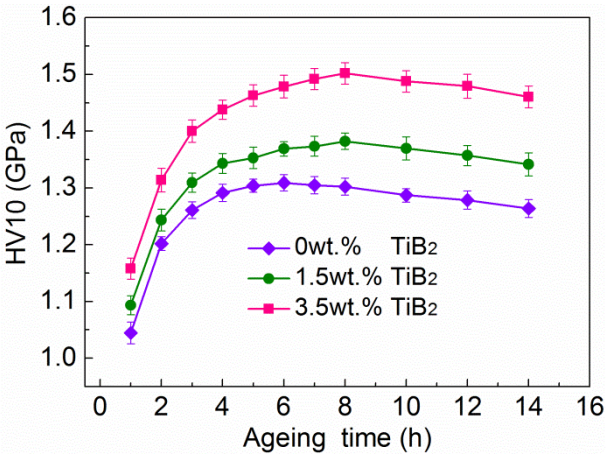

Fig. 8. Evolution of the hardness (HV10) of the die-cast Al–Si–Mg–Mn–TiB_2 composites versus ageing time after solution heat treatment.

Fig. 9 shows the evolution of the α–Al phase in the die-cast Al–Si–Mg–Mn–TiB_2 composites during heat treatment by EBSD analysis. Fig. 9a presents the inverse pole figure (IPF) orientation map showing the distribution of the α–Al phases in the as-cast composite reinforced by 3.5wt.% TiB_2, and the insert of the colour code in Fig. 9b represents the detail crystal orientation of the α–Al phases in Fig. 9a. Different α–Al phases can be easily distinguished by the difference of the orientation colour under IPF. From Fig. 9a, the relatively coarse primary α_1–Al and the fine secondary α_2–Al phase were also observed in the as-cast composite under IPF, which agreed with the observation in Fig. 4 under SEM. Fig. 9b shows the grain size distribution of the α–Al in the as-cast composite, the α_1–Al could be large as 30 μm, while the α_2–Al could be small as 3 μm. Fig. 9c presents the IPF orientation map showing the distribution of the α–Al phases in the 3.5wt.% TiB_2 reinforced composite

after solution and peak ageing heat treatment. The grain size of the α–Al phase in Fig. 9c was obviously coarser than that in Fig. 9a, which indicated that the α–Al phase was coarsened during heat treatment. Fig. 9d shows the grain size distribution of the α–Al phase in the 3.5wt.% TiB_2 reinforced composite after heat treatment, and it also verified the coarsening of α–Al during heat treatment, as the α–Al phase was shifted to direction of larger grain size. The combining of the neighbouring α–Al grains during the high temperature solution treatment at 540 °C led to the coarsening of the α–Al phase by diffusion. The coarsening of the α–Al phase during heat treatment was also reported by previous studies [35].

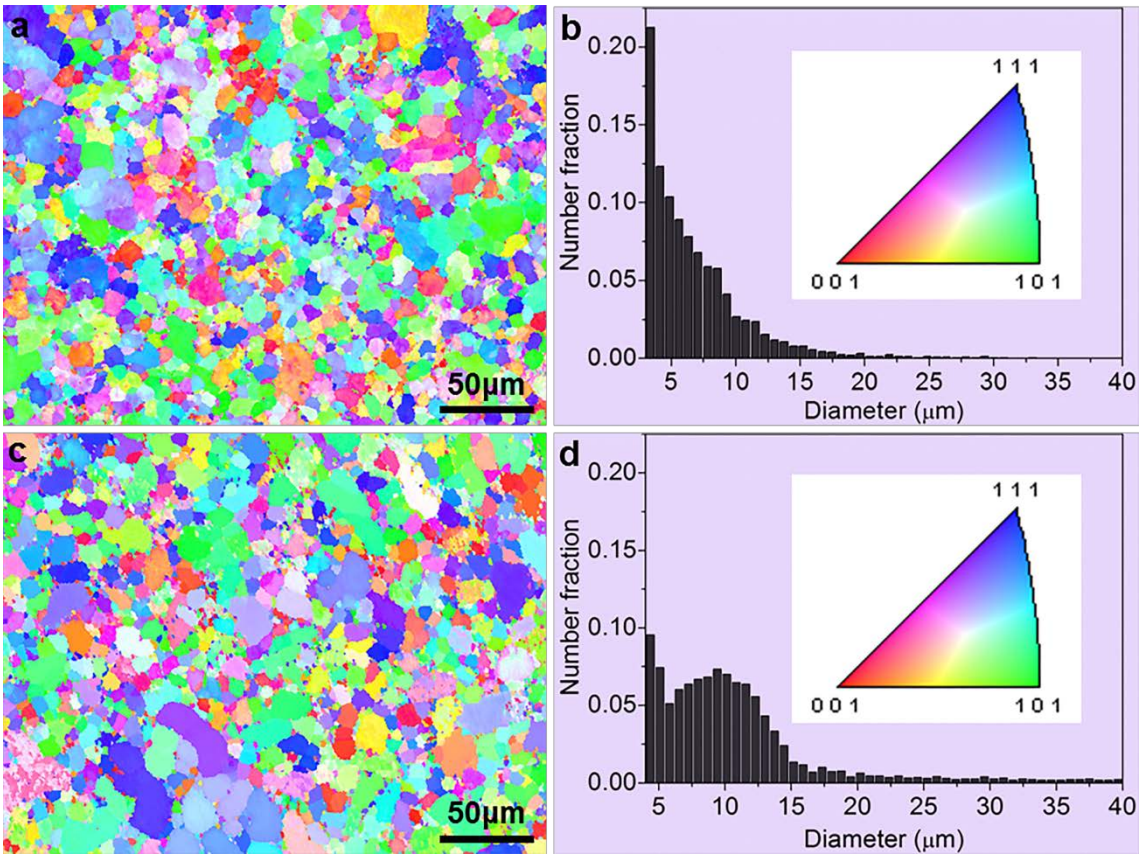

Fig. 9. EBSD results showing the evolution of the α–Al phase in the die-cast Al–Si–Mg–Mn–TiB_2 composites during heat treatment. (a) IPF orientation map and (b) grain size distribution of the α–Al phase in the as-cast composite reinforced by 3.5wt.% TiB_2, (c) IPF orientation map and (d) grain size distribution of the α–Al phase in the 3.5wt.% TiB_2 reinforced composite after solution and peak ageing heat treatment.

3.4. Heat-treated Al–Si–Mg–Mn–TiB_2 composites

3.4.1. Tensile properties

Fig. 10a presents the typical tensile stress-strain curves of the die-cast Al–Si–Mg–Mn–TiB_2 composites after solution and peak ageing heat treatment. With increasing content of TiB_2, the strength of the heat-treated composites increased, while the ductility decreased. Fig.

10b shows the tensile properties of the die-cast Al–Si–Mg–Mn–TiB_2 composites after solution and peak ageing heat treatment. The yield strength, ultimate tensile strength (UTS) and elongation (El) of the 0wt.% TiB_2 reinforced alloy were 317±2 MPa, 368±3 MPa and 11.6±0.9 %, respectively. The 1.5wt.% TiB_2 reinforced composite provided the high yield strength of 330±3 MPa and UTS of 384±3 MPa in conjunction with the ductility of 9.1±0.8 %, and the 3.5wt.% TiB_2 reinforced composite delivered the super high yield strength of 351±3 MPa and UTS of 410±4 MPa in association with the good ductility of 5.2±0.6 %. Never did literatures achieve die-cast aluminium alloys with the milestone high yield strength of 350 MPa in association with an industrially applicable ductility of 4 %. The super high yield strength of 351 MPa and UTS of 410 MPa in conjunction with the ductility of 5.2 % delivered by the present die-cast Al–Si–Mg–Mn–3.5wt.%TiB_2 composite are milestone mechanical properties for the high pressure die casting industry. In addition, the Al–Si–Mg–Mn–TiB_2 composites were proved having good die-cast capability within the addition of 3.5wt.% TiB_2 nanoparticles in Section 3.2.1, which made the present high performance die-cast Al–Si–Mg–Mn–TiB_2 composites promising for industrial application.

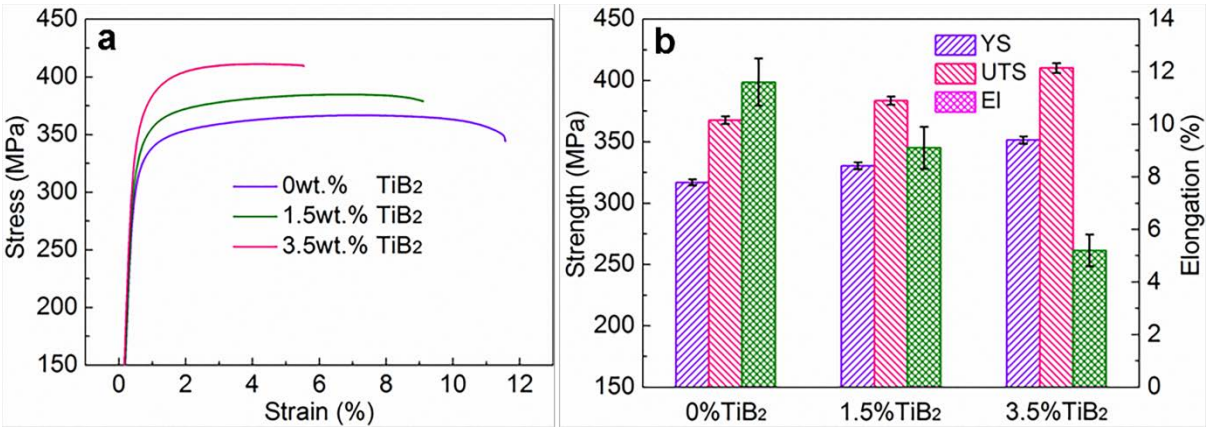

Fig. 10. (a) Tensile stress-strain curves and (b) tensile properties of the die-cast Al–Si–Mg–Mn–TiB_2 composites after solution and peak ageing heat treatment.

3.4.2. Microstructure and strengthening mechanism

The TEM images in Fig. 11 show the nanoscale precipitates in the α–Al matrix of the present die-cast alloy after solution and peak ageing treatment. Fig. 11a presents the bright-field TEM image taken along the non-zone axis of the α–Al matrix, and nanoscale β"–Mg_2Si precipitates dispersed homogeneously in the matrix of different α–Al phases. Fig. 11b shows the bright-field TEM image taken along the <001> zone axis of one α–Al grain, and embedded and lying β" nanoscale precipitates were observed dispersing uniformly in the α–Al matrix. The β" precipitate was reported in needle-like shape [39], and the embedded and

lying β" precipitates were the same β" precipitates in nature. Fig. 11c presents the HRTEM image of the embedded β" precipitate, and it clearly presented the unit cell of C-centered monoclinic structure with a = 1.52 nm and c = 0.67 nm, which verified that the embedded precipitate was β" [39,42,43], and the nanoscale β" precipitate was coherent with the α–Al matrix with Al[320]//β"(a-axis) and Al[1-30]//β"(c-axis). The fast Fourier transform (FFT) pattern in Fig. 11d also confirmed that the embedded precipitate in Fig. 11c was β". Fig. 11e shows the HRTEM image of the lying β" precipitate, and the β" precipitate had coherent interface with the α–Al matrix with Al[020]//β"(b-axis). The FFT pattern in Fig. 11f verified that the lying precipitate in Fig. 11e was β". The coherence between β" precipitate and the α–Al matrix resulted in excellent precipitation strengthening of the Al matrix.

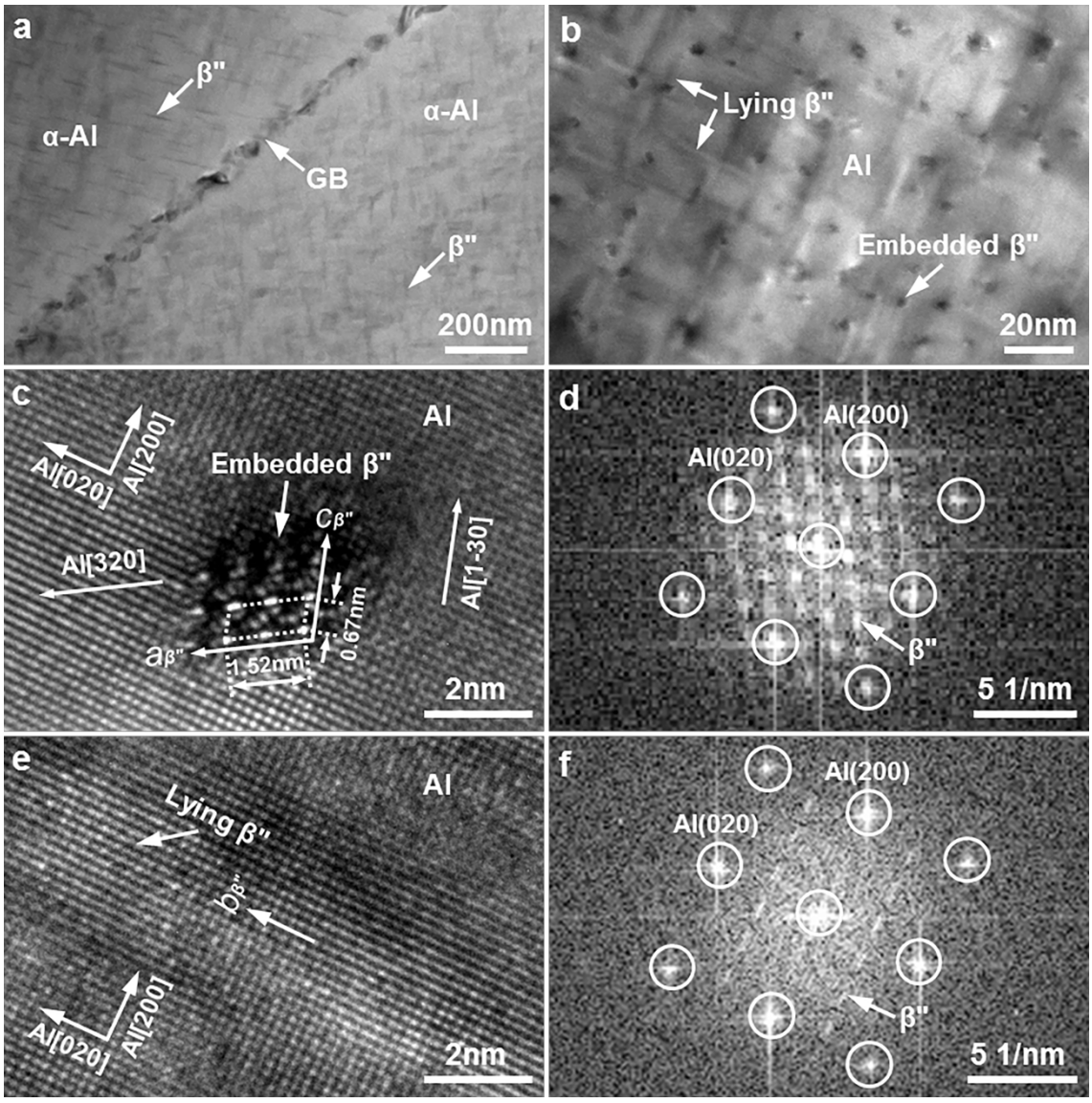

Fig. 11. TEM micrographs showing the nanoscale β" precipitate in the Al matrix of the die-cast Al–Si–Mg–Mn alloy after solution and peak ageing heat treatment. (a) Bright field image taken from non-zone axis of Al, (b) Bright field image taken along the <001> zone axis of Al, (c) HRTEM image of embedded

β" precipitate in (b), (d) FFT pattern of (c), (e) HRTEM image of lying β" precipitate in (b), (f) FFT pattern of (e).

Fig. 12 presents the TEM micrographs of the die-cast Al–Si–Mg–Mn–TiB_2 composites after solution and peak ageing heat treatment. Figs. 12a and b show the bright-field TEM images of the α–Al matrix of the 1.5wt.% TiB_2 reinforced composite, and TiB_2 nanoparticles and nanoscale β" precipitates were observed in the α–Al matrix, indicating that the α–Al matrix was double strengthened by the TiB_2 nanoparticles and nanoscale β" precipitates. Figs. 12c and d present the bright-field TEM images of the α–Al matrix of the 3.5wt.% TiB_2 reinforced composite, and the α–Al matrix of the 3.5wt.% TiB_2 reinforced composite was also double strengthened by the TiB_2 nanoparticles and nanoscale β" precipitates. The number density of the nanoscale β" precipitates in Fig. 12 seemed lower than that in Fig. 11, which was due to the difference of the observing direction under TEM. The morphology of the nanoscale β" precipitates was unclear when observing along the direction that the morphology of the TiB_2 nanoparticles was clear, and the number density of the nanoscale β" precipitates in the 0wt.% TiB_2, 1.5wt.% TiB_2 and 3.5wt.% TiB_2 reinforced composites was identical actually.

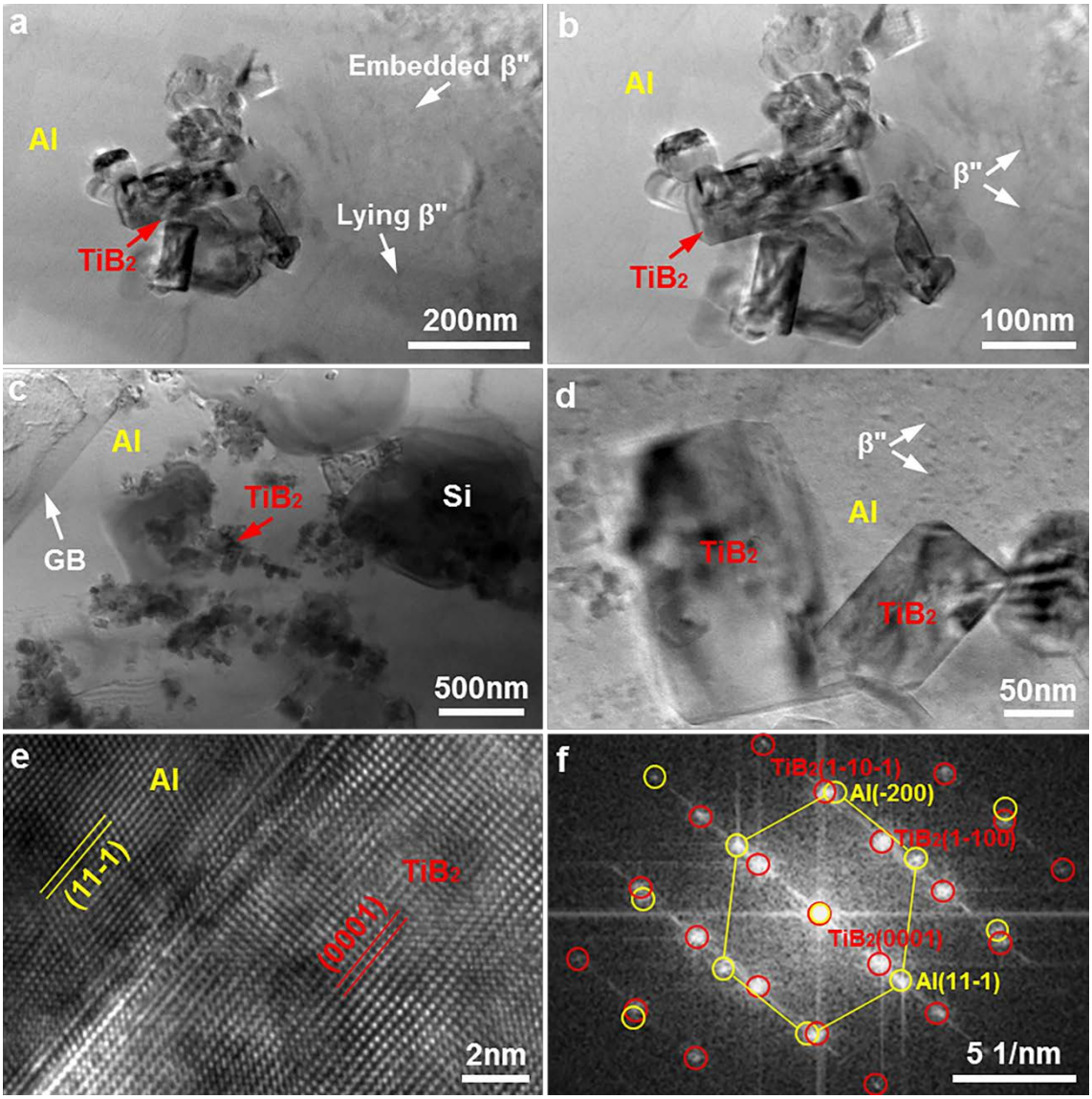

Fig. 12. TEM micrographs showing the nanoscale β" precipitate and TiB_2 nanoparticles in the Al matrix of the die-cast Al–Si–Mg–Mn–TiB_2 composites after solution and peak ageing heat treatment. Bright field images of the (a,b) 1.5wt.% and (c,d) 3.5wt.% TiB_2 reinforced composites, (e) HRTEM image and (f) FFT pattern showing the interface and orientation relation between the middle TiB_2 nanoparticle and the Al matrix in (d).

From Fig. 6, the TiB_2 nanoparticles distributed in the grain boundary rather than the α–Al matrix of the 1.5wt.% and 3.0wt.% TiB_2 reinforced composites in as-cast state. The α–Al phases in the heat-treated composite were coarser than that in the as-cast composite, as verified by the EBSD analysis in Fig. 9, which indicated that the nearby α–Al phases in as-cast state were combined and coarsened during the subsequent high temperature solution heat treatment at 540 °C by diffusion. The TiB_2 nanoparticles in the grain boundary of the as-cast composite were therefore enrolled into the α–Al matrix of heat-treated composite through the combining and coarsening of the α–Al phases during the solution heat treatment. Fig. 12e

presents the HRTEM image showing the interface between the middle TiB_2 nanoparticle and the α–Al matrix in Fig. 12d, and the TiB_2 nanoparticle was found having coherent interface with the α–Al matrix, with the (0001) crystal plane of the TiB_2 nanoparticle parallel to the (11-1) crystal plane of the α–Al matrix, which indicated strong interfacial bonding and strengthening. The FFT pattern in Fig. 12f revealed that the crystal orientation relation (OR) between the TiB_2 nanoparticle and the α–Al matrix was Al(11-1)//TiB_2(0001) and Al[011]//TiB2[11-20], and this OR agreed with previous reports [41,44]. Thus the die-cast Al–Si–Mg–Mn–TiB_2 composites were double strengthened by the TiB_2 nanoparticles and the nanoscale β" precipitates that both had coherent interfaces with the α–Al matrix, which resulted in the high strength of the present composites.

3.4. Fracture mechanism

Fig. 13 shows the SEM micrographs of the tensile fracture surface of the die-cast Al–Si–Mg–Mn–TiB_2 composites, after solution and peak ageing heat treatment. Fig. 13a presents the SEM morphology of the fracture of the 0wt.% TiB_2 reinforced alloy, Al dimples were found distributing uniformly across the fracture indicating the ductile fracture, which agreed with the good ductility of the alloy. Cracks were observed originating from the Si phase due to its brittle feature [25,33]. Fig. 13b shows the SEM morphology of the fracture of the 1.5wt.% TiB_2 reinforced composite, and TiB_2 nanoparticles were observed on the fracture. Crack was still found in the Si phase in the fracture, and the number of the Al dimples in the fracture decreased comparing with the 0wt.% TiB_2 reinforced alloy, which was consistent with the decrease of the ductility of the composite. Figs. 13c and d present the SEM morphology of the fracture of the 3.5wt.% TiB_2 reinforced composite, and it also comprised the Al dimples, the cracked Si phase and the TiB_2 nanoparticles. However, the number of the Al dimples decreased further due to the increase of the TiB_2 nanoparticles in the fracture, which led to the further decrease of the ductility of the composite. The increase of the hard TiB_2 ceramic reinforcement nanoparticles accelerated the crack of the brittle Si phase under stretching, due to the strong interaction of the hard TiB_2 nanoparticles and the brittle Si phase, and this led to the decrease of the ductility of the composites with increasing addition of TiB_2 nanoparticles.

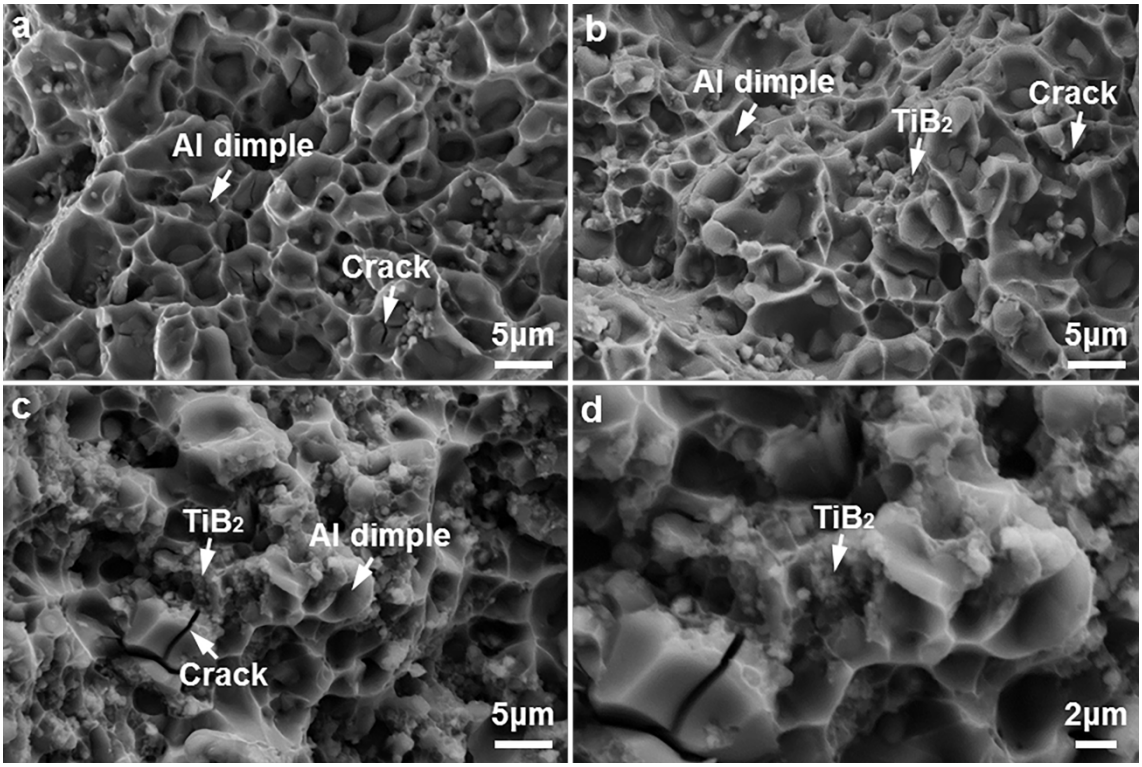

Fig. 13. SEM morphology of the tensile fracture surface of the die-cast Al–Si–Mg–Mn–TiB_2 composites after solution and peak ageing heat treatment. (a) 0wt.% TiB_2 reinforced alloy, (b) 1.5wt.% TiB_2 reinforced composite, (c,d) 3.5wt.% TiB_2 reinforced composite.

4. Conclusions （结论部分也要改，你这也是工艺文章的套路，改成机理文章的。因为你是想告诉别人强度的增加原因。）

(1) Advanced die-cast Al–Si–Mg–Mn–TiB_2 composites were fabricated with milestone high yield strength of above 350 MPa and an industrially applicable ductility of over 4 %, through the reinforcement of TiB_2 nanoparticles and the super vacuum assisted high pressure die casting process. The compsites beared good die-cast capability within the addtion of 3.5wt.% TiB_2 nanoparticles.

(2) The 3.5wt.% TiB_2 nanoparticle reinforced die-cast Al–Si–Mg–Mn–TiB_2 composite delivered the super high hardness of 1.5 GPa, the milestone high yield strength of 351±3 MPa and ultimate tensile strength of 410±4 MPa in association with a good ductility of 5.2±0.6 %, after solution and peak ageing heat treatment.

(3) The TiB_2 nanoparticles distributed in the grain boundary rather than in the α–Al matrix phase of the die-cast Al–Si–Mg–Mn–TiB_2 composites in as-cast state. After solution and peak ageing heat treatment, the TiB_2 nanoparticles were enrolled into the α–Al matrix phase through the combining and coarsening of the α–Al phase during heat treatment.

(4) The α–Al matrix of the solution and peak aged die-cast Al–Si–Mg–Mn–TiB_2 composites were double strengthened by the TiB_2 nanoparticles and the nanoscale β" precipitates that both had coherent interfaces with α–Al, which resulted in the milestone high strength of the composites. The TiB_2 nanoparticles were coherent with Al matrix with Al(11-1)//TiB_2(0001) and Al[011]//TiB2[11-20], and the nanoscale β" precipitates were coherent with Al matrix with Al[320]//β"(*a*-axis), Al[1-30]//β"(*c*-axis) and Al(020)//β"(*b*-axis).

Acknowledgements

Financial support from Innovate UK under project 131817 is gratefully acknowledged.

References

[1] L. Wang, M. Makhlouf, D. Apelian, Aluminium die casting alloys: alloy composition, microstructure, and properties-performance relationships, Int. Mater. Rev. 40 (1995) 221–238.

[2] X.X. Dong, X.S. Huang, L.H. Liu, L.J. He, P.J. Li, A liquid aluminum alloy electromagnetic transport process for high pressure die casting, J. Mater. Process. Technol. 234 (2016) 217–227.

[3] H.L. Yang, S. Ji, W.C. Yang, Y. Wang, Z. Fan, Effect of Mg level on the microstructure and mechanical properties of die–cast Al–Si–Cu alloys, Mater. Sci. Eng. A 642 (2015) 340–350.

[4] X.X. Dong, G.B. Mi, L.J. He, P.J. Li, 3D simulation of plane induction electromagnetic pump for the supply of liquid Al-Si alloys during casting, J. Mater. Process. Technol. 213 (2013) 1426–1432.

[5] X. Li, S.M. Xiong, Z. Guo, Correlation between porosity and fracture mechanism in high pressure die casting of AM60B alloy, J. Mater. Sci. Technol. 32 (2016) 54–61.

[6] X.X. Dong, L.J. He, X.S. Huang, P.J. Li, Coupling analysis of the electromagnetic transport of liquid aluminum alloy during casting, J. Mater. Process. Technol. 222 (2015) 197–205.

[7] L.H. Wang, P. Turnley, G. Savage, Gas content in high pressure die castings, J. Mater. Process. Technol. 211 (2011) 1510–1515.

[8] X.X. Dong, L.J. He, X.S. Huang, P.J. Li, Effect of electromagnetic transport process on the improvement of hydrogen porosity in A380 aluminum alloy, Int J Hydrogen Energy 40 (2015) 9287–9297.

[9] S. Ji, F. Yan, Z.Y. Fan, Development of a high strength Al–Mg_2Si–Mg–Zn based alloy for high pressure die casting, Mater. Sci. Eng. A 626 (2015) 165–174.

[10] Y. Zhang, J.B. Patel, J. Lazaro-Nebreda, Z. Fan, Improved defect control and mechanical property variation in high-pressure die casting of A380 alloy by high shear melt conditioning, JOM 70 (2018) 2726–2730.

[11] Z.Q. Hu, L. Wan, S.S. Wu, H. Wu, X.Q. Liu, Microstructure and mechanical properties of high strength die-casting Al–Mg–Si–Mn alloy, Mater. Des. 46 (2013) 451–456.

[12] P. Zhang, Z.M. Li, B.L. Liu, W.J. Ding, Effect of chemical compositions on tensile behaviors of high pressure die-casting alloys Al-10Si-yCu-xMn-zFe, Mater. Sci. Eng. A 661 (2016) 198–210.

[13] X.Z. Zhu, P. Blake, K. Dou, S. Ji, Strengthening die-cast Al-Mg and Al-Mg-Mn alloys with Fe as a beneficial element, Mater. Sci. Eng. A 732 (2018) 240–250.

[14] L.Y. Yuan, L.M. Peng, J.Y. Han, B.L. Liu, Y.J. Wu, J. Chen, Effect of Cu addition on microstructures and tensile properties of high-pressure die-casting Al-5.5Mg-0.7Mn alloy, J. Mater. Sci. Technol. 35 (2019) 1017–1026.

[15] D.J. Lloyd, Particle reinforced aluminium and magnesium matrix composites, Int. Mater. Rev. 39 (1994) 1–23.

[16] L.Y. Chen, J.Q. Xu, H. Choi, M. Pozuelo, X.L. Ma, S. Bhowmick, J.M. Yang, S. Mathaudhu, X.C. Li, Processing and properties of magnesium containing a dense uniform dispersion of nanoparticles, Nature 528 (2015) 539–543.

[17] Y.W. Shen, X.F. Li, T.R. Hong, J.W. Geng, H.W. Wang, Effects of TiB_2 particles on microstructure and mechanical properties of an in-situ TiB_2-Al–Cu–Li matrix composite, Mater. Sci. Eng. A 655 (2016) 265–268.

[18] S.A. Sajjadi, H.R. Ezatpour, H. Beygi, Microstructure and mechanical properties of Al–Al_2O_3 micro and nano composites fabricated by stir casting, Mater. Sci. Eng. A 528 (2011) 8765–8771.

[19] Z.Y. Ma, Y.L. Li, Y. Liang, F. Zheng, J. Bi, S.C. Tjong, Nanometric Si_3N_4 particulate-reinforced aluminum composite, Mater. Sci. Eng. A 219 (1996) 229–231.

[20] K. Kalaiselvan, N. Murugan, S. Parameswaran, Production and characterization of AA6061–B_4C stir cast composite, Mater. Des. 32 (2011) 4004–4009.

[21] S. Jerome, B. Ravisankar, P.K. Mahato, S. Natarajan, Synthesis and evaluation of mechanical and high temperature tribological properties of in-situ Al–TiC composites, Tribol. Int. 43 (2010) 2029–2036.

[22] S.M.S. Reihani, Processing of squeeze cast Al6061-30vol% SiC composites and their characterization, Mater. Des. 27 (2006) 216–222.

[23] Q.Y Hu, H.D. Zhao, F.D. Li, Microstructures and properties of SiC particles reinforced aluminum–matrix composites fabricated by vacuum–assisted high pressure die casting, Mater. Sci. Eng. A 680 (2017) 270–277.

[24] R.G. Munro, Material properties of titanium diboride, J. Res. Natl. Inst. Stand. Technol. 105 (2000) 709–720.

[25] X.X. Dong, X.Z. Zhu, S. Ji, Effect of super vacuum assisted high pressure die casting on the repeatability of mechanical properties of Al-Si-Mg-Mn die-cast alloys, J. Mater. Process. Technol. 266 (2019) 105–113.

[26] X.P. Niu, B.H. Hu, I. Pinwill, H. Li, Vacuum assisted high pressure die casting of aluminium alloys, J. Mater. Process. Technol. 105 (2000) 119–127.

[27] X.J. Wang, S.M. Zhu, M.A. Easton, M.A. Gibson, G. Savage, Heat treatment of vacuum high pressure die cast magnesium alloy AZ91, Int J Cast Metal Res. 27 (2014) 161–166.

[28] X.Y. Shi, D.J. Li, A.A. Luo, B. Hu, L. Li, X.Q. Zeng, W.J. Ding, Microstructure and mechanical properties of Mg-7Al-2Sn alloy processed by super vacuum die-casting, Metall. Mater. Trans A 44 (2013) 4788–4799.

[29] Q.L. Wang, S.M. Xiong, Vacuum assisted high-pressure die casting of AZ91D magnesium alloy at different slow shot speeds, Trans. Nonferrous Met. Soc. China 24 (2014) 3051–3059.

[30] X.X. Dong, S.X. Ji, Si poisoning and promotion on the microstructure and mechanical properties of Al–Si–Mg cast alloys, J Mater. Sci. 53 (2018) 7778–7792.

[31] M. Javidani, D. Larouche, Application of cast Al–Si alloys in internal combustion engine components, Int. Mater. Rev. 59 (2014) 132–158.

[32] X.X. Dong, L.J. He, G.B. Mi, P.J. Li, Two directional microstructure and effects of nanoscale dispersed Si particles on microhardness and tensile properties of AlSi7Mg melt-spun alloy, J. Alloy Compd. 618 (2015) 609–614.

[33] X.X. Dong, Y.J. Zhang, S.X. Ji, Enhancement of mechanical properties in high silicon gravity cast AlSi9Mg alloy refined by Al3Ti3B master alloy, Mater. Sci. Eng. A 700 (2017) 291–300.

[34] F. Yan, W.C. Yang, S.X. Ji, Z.Y. Fan, Effect of solutionising and ageing on the microstructure and mechanical properties of a high strength die-cast Al–Mg–Zn–Si alloy, Mater. Chem. Phys. 167 (2015) 88–96.

[35] X.X. Dong, H.L. Yang, X.Z. Zhu, S. Ji, High strength and ductility aluminium alloy processed by high pressure die casting, J. Alloys Compd. 773 (2019) 86–96.

[36] S. Lakshmi, L. Lu, M. Gupta, In situ preparation of TiB_2 reinforced Al based composites, J. Mater. Process. Technol. 73 (1998) 160–166.

[37] A. Abdel-Hamid, S. Hamar-Thibault, R. Hamar, Crystal morphology of the compound TiB_2, J. Cryst. Growth 71 (1985) 744–750.

[38] X.X. Dong, Y.J. Zhang, S. Amirkhanlou, S.X. Ji, High performance gravity cast Al9Si0.45Mg0.4Cu alloy inoculated with AlB_2 and TiB_2, J. Mater. Process. Technol. 252 (2018) 604–611.

[39] S.J. Andersen, H.W. Zandbergen, J. Jansen, C. Traeholt, U. Tundal, O. Reiso, The crystal structure of the β" phase in Al–Mg–Si alloys, Acta Mater. 46 (1998) 3283–3298.

[40] Z.P. Que, Y. Wang, Z. Fan, Formation of the Fe-Containing Intermetallic Compounds during Solidification of Al-5Mg-2Si-0.7Mn-1.1Fe Alloy, Metall. Mater. Trans. A 49 (2018) 2173–2181.

[41] X.P. Li, G. Ji, Z. Chen, A. Addad, Y. Wu, H.W. Wang, J. Vleugels, J. Van Humbeeck, J.P. Kruth, Selective laser melting of nano-TiB_2 decorated AlSi10Mg alloy with high fracture strength and ductility, Acta Mater. 129 (2017) 183–193.

[42] W.C. Yang, M.P. Wang, R.R. Zhang, Q. Zhang, X.F. Sheng, The diffraction patterns from β" precipitates in 12 orientations in Al–Mg–Si alloy, Scr. Mater. 62 (2010) 705–708.

[43] W.C. Yang, S.X. Ji, L.P. Huang, X.F. Sheng, L. Zhou, M.P. Wang, Initial precipitation and hardening mechanism during non-isothermal aging in an Al-Mg-Si-Cu 6005A alloy, Mater. Charact. 94 (2014) 170–177.

[44] Z. Fan, Y. Wang, Y. Zhang, T. Qin, X.R. Zhou, G.E. Thompson, T. Pennycook, T. Hashimoto, Grain refining mechanism in the Al/Al–Ti–B system, Acta Mater. 84 (2015) 292–304.